Two-Step Solvothermal Process for Nanoarchitectonics of Metastable Hexagonal WO_3 Nanoplates

Qiu, Zanlin; Jinschek, Joerg R.; Gouma, Pelagia Irene

Published in:
Crystals

Link to article, DOI:
10.3390/cryst13040690

Publication date:
2023

Document Version
Publisher's PDF, also known as Version of record

crystals

MDPI

Article

Two-Step Solvothermal Process for Nanoarchitectonics of Metastable Hexagonal WO_3 Nanoplates

Zanlin Qiu [1], Joerg R. Jinschek [2] and Pelagia-Irene Gouma [1,3,*]

[1] Department of Materials Science and Engineering, The Ohio State University, Columbus, OH 43210, USA; qiu.512@osu.edu
[2] National Centre for Nano Fabrication and Characterization, Denmark Technical University, DK-2800 Kongens Lyngby, Denmark; jojin@dtu.dk
[3] Department of Mechanical and Aerospace Engineering, The Ohio State University, Columbus, OH 43202, USA
* Correspondence: gouma.2@osu.edu; Tel.: +1-614-292-4391

Abstract: Hexagonal tungsten trioxide (h-WO_3) has shown great potential for application in electrochromic devices, gas sensors, battery electrodes, and as photo-catalysts. The h-WO_3 structure features a unique large network of open hexagonal channels that allow for intercalation. The hydrothermal synthesis of h-WO_3 using sodium tungstate dihydrate as a precursor is widely explored, however, the residual alkaline ions are difficult to eliminate during the synthesis. The solvothermal synthesis using tungsten hexachloride as starting materials largely avoids the use of alkaline ions, but the effect of various synthesis parameters is not well-understood yet. To resolve these ambiguities, this study provides a reliable route to obtain h-WO_3 via solvothermal synthesis and dehydration annealing. The effects of precursor concentration, water content, synthesis temperature, and synthesis time, as well as dehydration temperature, on the as-synthesized crystal structure and crystal morphology are studied.

Keywords: hexagonal tungsten trioxide; solvothermal synthesis; crystal structure; crystal morphology

check for updates

Citation: Qiu, Z.; Jinschek, J.R.; Gouma, P.-I. Two-Step Solvothermal Process for Nanoarchitectonics of Metastable Hexagonal WO_3 Nanoplates. *Crystals* **2023**, *13*, 690. https://doi.org/10.3390/cryst13040690

Academic Editors: Helmut Cölfen, Abdullah Mohamed Asiri and Andrei Vladimirovich Shevelkov

Received: 26 March 2023
Revised: 5 April 2023
Accepted: 14 April 2023
Published: 17 April 2023

1. Introduction

Tungsten trioxide (WO_3) is a polymorph material, and the various crystalline polymorphs of WO_3 are either stable or metastable. According to previous studies [1–3], at least five traditional polymorphs for bulk WO_3 have been reported: ε-WO_3 (space group: Pc), δ-WO_3 (P1), γ-WO_3 ($P2_1/n$), β-WO_3 (Pbcn), and α-WO_3 (P4/ncc). Further, a metastable hexagonal polymorph (h-WO_3, P6/mmm) that exhibits a large network of open hexagonal channels along the *c*-axis has been reported [3–31]. It has been shown that this characteristic of h-WO_3 opens a wide range of applications in electrochemical, as well as in electrochromic appliances [6,7], as gas sensors [7–10] and in photo-catalysis [11,12].

The h-WO_3 was first synthesized using an acid precipitation method of sodium tungstate dihydrate [4]. Over the years, researchers have shown that h-WO_3 can be obtained by a variety of methods: by hydrothermal treatment of alkaline tungstate hydrates [13–19], by hydrothermal treatment of peroxopolytungstic acid [20], by oxidation of ammonium tungsten bronze [4,21,22], by sol–gel methods [23–26], by dehydration of $WO_3 \cdot 0.33(H_2O)$ [27–29], by spray pyrolysis [32], or by solvothermal synthesis using tungsten hexachloride (WCl_6) as precursor [30,31]. Among these methods, hydrothermal synthesis with alkaline tungstate hydrates as precursor is most commonly used because of its tunability to control particle size and morphology ranging from nanoparticle, nanowire, and nanosheet, to nanotube. The crystal structure of the product powder during hydrothermal synthesis is significantly influenced by the pH value during synthesis [13–19]. Several previous studies have shown that h-WO_3 can be synthesized at pH values between 1.5 to 2.3 [13–16,18,19]. Ahmadian et al. [17] has shown that pH 2 and pH 4 can stabilize h-WO_3, while at pH 3, $WO_3 \cdot 0.5(H_2O)$ is dominant. In addition to pH, the presence of alkaline

ions or ammonium ions is believed to play a role in stabilizing h-WO_3 [4,33]. As for the particle morphology of h-WO_3, several articles have shown that this is largely controlled by the templates, capping agent, or structure-directing agents (SDA), such as sodium sulfate, potassium sulfate, oxalic acid, ferrous ammonium sulfate, sodium chloride, and cobalt chloride [11,18,34–37].

It is also feasible to obtain h-WO_3 by first obtaining $WO_3 \cdot 0.33(H_2O)$ from hydrothermal synthesis and then dehydration by subsequent annealing [4,22,27–29]. Marques et al. [18] suggested that $WO_3 \cdot 0.33(H_2O)$ can be synthesized at pH 0.4–1.8, depending on the types of SDA. Seguin et al. [28] studied the dehydration process of $WO_3 \cdot 0.33(H_2O)$ and found that $WO_3 \cdot 0.33(H_2O)$ first transforms to a super-metastable WO_3 phase at about 350 °C and subsequently transforms to h-WO_3 at around 380 °C. However, when the temperature reaches ~500 °C, h-WO_3 transforms into thermostable γ-WO_3 [28]. The exact temperature for this transition depends on the composition of h-WO_3 (e.g., sodium content, ammonium ions content, and so on) [22].

A major challenge in hydrothermal treatment is the difficulty in controlling the amount of alkaline ions or ammonium ions in h-WO_3 [4]. These ions originate from precursors or SDA and are believed to play a role in stabilizing h-WO_3 [4,20,33]. In other words, it seems impossible to obtain pure h-WO_3 from hydrothermal synthesis. Solvothermal synthesis using WCl_6 as precursor can obtain h-WO_3 free from alkaline ions [8,30,31]. Choi et al. [30] has shown that h-WO_3 can be directly synthesized by solvothermal synthesis with WCl_6 as precursor and a water/ethanol mixture solution as solvent with a water content between 2 vol% and 10 vol%. However, Chacón et al. [31] point out that the solvothermal synthesis product is $WO_3 \cdot 0.33(H_2O)$ rather than h-WO_3 under the condition mentioned in Choi et al. (i.e., $[WCl_6]$ = 0.0125 M–0.014 M, $[H_2O]$ = 10 vol%) [30]. Also, the effects of precursor concentration, reaction temperature, and reaction time are still not well-understood yet.

To address these open questions, we here present a systematical study on solvothermal synthesis using WCl_6 as precursor and a mixed water/ethanol solution as the solvent. The effects of parameters such as water concentration, precursor concentration, synthesis temperature, synthesis time, as well as annealing temperature, are studied systematically. The results show that the solvothermal synthesis product can be either $W_{18}O_{49}$, $WO_3 \cdot 0.33(H_2O)$ or γ-WO_3 depending on precursor concentration and water content. h-WO_3 is not observed in the powder produced from solvothermal synthesis, but it is obtained by subsequently annealing the $WO_3 \cdot 0.33(H_2O)$ at 400–450 °C.

2. Materials and Methods

2.1. Materials Synthesis

The materials synthesis procedure is shown in Figure 1. The starting solution was prepared by dissolving 4.9575 g WCl_6 (Sigma-Aldrich, St. Louis, MO, USA) into 125 mL of anhydrous ethanol (Neta scientific Inc, Hainesport, NJ, USA) in an argon-filled glove box to prevent hydration of the WCl_6 ($[WCl_6]$ = 0.1 M). The solution immediately turned yellow as HCl vapor escaped from the container. Eventually, the solution turned blue, ultimately reaching a deep green color after one week. Based on previous studies [38], the final (green) solution is a $W_2Cl_4(OC_2H_5)_6$ solution. For convenience, we still use $[WCl_6]$ to denote the precursor concentration in this study, although WCl_6 has been transformed to $W_2Cl_4(OC_2H_5)_6$.

The final solution was prepared by mixing $W_2Cl_4(OC_2H_5)_6$ solution (starting solution), anhydrous ethanol, and distilled water under magnetic stirring for 3 h. In order to prepared the final solution with different precursor concentration ($[WCl_6]$ = 0.01 M or 0.05 M) and different water content (0 vol%, 5 vol%, 10 vol%, 20 vol%, or 50 vol%), the volumes of the $W_2Cl_4(OC_2H_5)_6$ solution (starting solution), the final solution, and of the distilled water are listed in Table 1. Then, the final solution was sealed, removed from the argon-filled glovebox and was transferred into a 100 mL Teflon-lined hydrothermal pressure vessel. The solvothermal synthesis was conducted at 200 °C for 12 h in an electric oven. After that,

the as-synthesized material was centrifuged and washed with ethanol several times. The powder was then allowed to dry at room temperature in a fume hood.

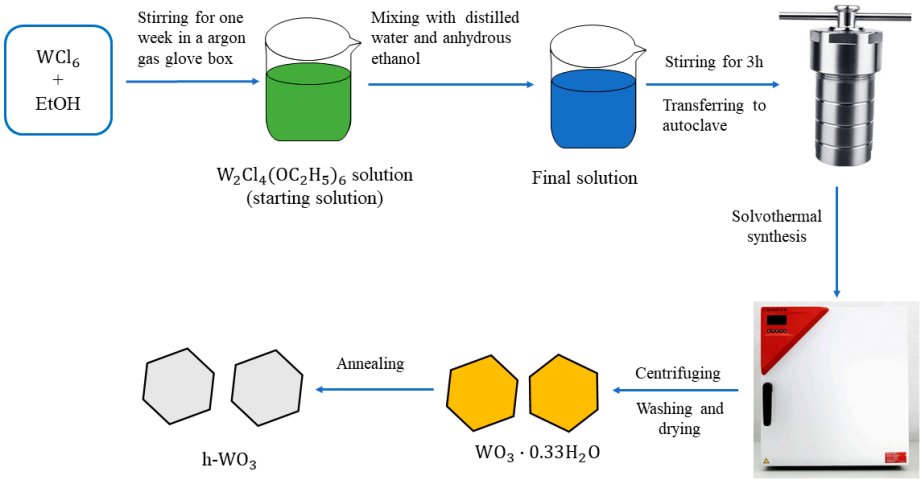

Figure 1. Schematic of solvothermal synthesis procedure.

Table 1. Details of samples 1–10: list of volumes of the $W_2Cl_4(OC_2H_5)_6$ solution (starting solution), the final solution, and the distilled water.

Sample No.	$V_{starting\ solution}$	$V_{final\ solution}$	V_{water}	[WCl_6] for Final Solution	Water Content	Synthesis Temperature	Synthesis Time
1	5 mL	50 mL	0 mL	0.01 M	0 vol%	200 °C	12 h
2	5 mL	50 mL	2.5 mL	0.01 M	5 vol%	200 °C	12 h
3	5 mL	50 mL	5 mL	0.01 M	10 vol%	200 °C	12 h
4	5 mL	50 mL	10 mL	0.01 M	20 vol%	200 °C	12 h
5	5 mL	50 mL	25 mL	0.01 M	50 vol%	200 °C	12 h
6	25 mL	50 mL	0 mL	0.05 M	0 vol%	200 °C	12 h
7	25 mL	50 mL	2.5 mL	0.05 M	5 vol%	200 °C	12 h
8	25 mL	50 mL	5 mL	0.05 M	10 vol%	200 °C	12 h
9	25 mL	50 mL	10 mL	0.05 M	20 vol%	200 °C	12 h
10	25 mL	50 mL	25 mL	0.05 M	50 vol%	200 °C	12 h

To study the effect of synthesis temperature and time on the synthesis of $WO_3{\cdot}0.33(H_2O)$, 50 mL of final solution containing 0.01 M of [WCl_6] and a water content of 10 vol% was prepared. Then, the solvothermal synthesis was conducted at temperatures between 160 °C and 200 °C and synthesis times between 3 h and 12 h, as listed in Table 2.

To study the dehydration process of $WO_3{\cdot}0.33(H_2O)$, the $WO_3{\cdot}0.33(H_2O)$ powders (sample no.3) were characterized by thermal gravimetric analysis (TGA) in an argon gas environment. The TGA temperature ranged from room temperature to 750 °C, using a heating rate of 5 °C/min. The annealing experiments were conducted in an electric oven using sample no.3 as a starting material. The annealing temperatures were 300 °C, 350 °C, 400 °C, 450 °C, 500 °C, and 550 °C. Annealing time was set to 2 h.

Table 2. Details of the solvothermal synthesis: list of applied synthesis temperatures and times. For convenience, we use [WCl_6] to denote precursor concentration.

Sample No.	$V_{starting\ solution}$	$V_{final\ solution}$	V_{water}	[WCl_6] for Final Solution	Water Content	Synthesis Temperature	Synthesis Time
11	5 mL	50 mL	5 mL	0.01 M	10 vol%	160 °C	12 h
12	5 mL	50 mL	5 mL	0.01 M	10 vol%	180 °C	12 h
13	5 mL	50 mL	5 mL	0.01 M	10 vol%	200 °C	3 h
14	5 mL	50 mL	5 mL	0.01 M	10 vol%	200 °C	6 h
15	5 mL	50 mL	5 mL	0.01 M	10 vol%	200 °C	9 h

2.2. Materials Characterization

The X-ray powder diffraction (XRD) data were collected using a Rigaku SmartLab diffractometer with a Cu Kα radiation source (λ = 1.5418 Å) at a scan rate of 1° min^{-1} in the 2θ range from 10° to 40°. The morphologies of the samples were investigated using scanning electron microscopy (SEM, Thermo scientific Quattro ESEM) and transmission electron microscopy (TEM, FEI Tecnai G2 at 200 kV). To identify the structure of each powder, selected area electron diffraction (SAED) and high-resolution TEM (HRTEM) characterization was performed.

3. Results

3.1. Effects of Water Content and Precursor Concentration on Crystal Structure of As-Synthesized Powder

The results of the X-ray diffraction (XRD) experiments on samples 1–5 are shown in Figure 2. The XRD pattern of powder synthesized under pure ethanol condition (sample 1) has a strongest diffraction peak at 23.32° that can be assigned to $W_{18}O_{49}$ (JCPDS no. 36-0101). The other characteristic peaks of $W_{18}O_{49}$ are not observed due to the strong broadening effect, which is commonly observed in the XRD spectra of nanocrystalline materials. The XRD data in Figure 2 suggests that the addition of water into the solvent stabilizes $WO_3{\cdot}0.33(H_2O)$ and γ-WO_3. Specifically, when the water content is 5 vol% (sample 2) and 10 vol% (sample 3), respectively, the XRD patterns exhibit diffraction peaks at 13.96°, 18.1°, 22.98°, 24.26°, 27.04°, and 28.18°, respectively (JCPDS no. 87-1203). All these observed peaks correspond to diffraction peaks of $WO_3{\cdot}0.33(H_2O)$. Some minor peaks of γ-WO_3 phases are also observed (at 23.6°, 26.12°), but the intensity is extremely low, suggesting that $WO_3{\cdot}0.33(H_2O)$ is the dominant phase in sample 2 and sample 3. Several other studies about solvothermal synthesis at similar water and precursor concentrations have suggested before that $WO_3{\cdot}0.33(H_2O)$ is the product without any further heat treatment [31,39]. However, both our and these previous results are in conflict with the results of Choi et al. [30], in which pure hexagonal phase is directly synthesized under this condition ([WCl_6] = 0.0125 M–0.014 M, [H_2O] = 10 vol%).

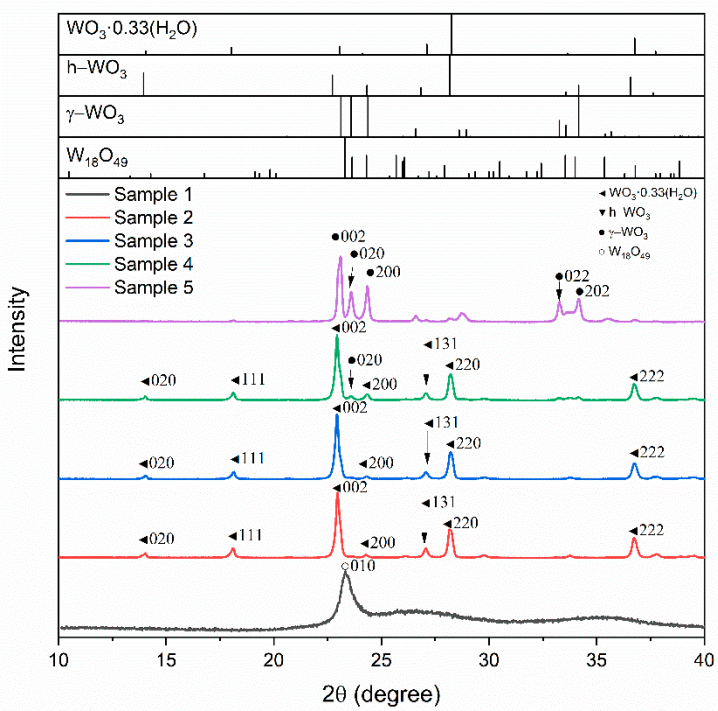

Figure 2. XRD data of samples 1–5 (see details in Table 1). For comparison: the top inset is the standard reference diffraction patterns of $W_{18}O_{49}$ (JCPDS no. 36-0101), h-WO_3 (JCPDS no. 75-2187), $WO_3{\cdot}0.33(H_2O)$ (JCPDS no. 87-1203), and γ-WO_3 (JCPDS no. 32-1295).

One possible explanation for the discrepancy between our work and Choi et al. [30] is that the latter did not distinguish the XRD patterns of $WO_3 \cdot 0.33(H_2O)$ and h-WO_3. Specifically, only the XRD peaks at 18.1°, 22.78°, and 22.98° can be used to identify these two compounds based on XRD pattern analysis. Since the XRD pattern in Choi et al. [30] was acquired at a 2θ range from 20° to 45°, it does not include the characteristic peaks of $WO_3 \cdot 0.33(H_2O)$ at 18.1°. Also, the 001 peak of "hexagonal WO_3" in Choi et al. [30] is at 23° ± 0.1°, which should have been indexed as 002 peak of $WO_3 \cdot 0.33(H_2O)$ rather than the 001 peak of h-WO_3 (at 22.78°).

Further increase in water content to 20 vol% (sample 4) or 50 vol% (sample 5) results in the formation of γ-WO_3, as suggested by the appearance of XRD peaks at 23.12°, 23.6°, 24.34°, 26.12°, 33.28°, and 34.14° in Figure 2 (JCPDS no. 32-1295). The powder synthesized using a water content of 20 vol% consists of $WO_3 \cdot 0.33(H_2O)$ and a small amount of γ-WO_3 as suggested by the strong $WO_3 \cdot 0.33(H_2O)$ diffraction peaks and weak γ-WO_3 peak at 23.1°. However, when water content is increased to 50 vol%, γ-WO_3 becomes dominate, in agreement with results published by Chacón et al. [31].

When the precursor concentration is increased to 0.05 M, a totally different situation emerges. Figure 3 shows the XRD patterns of powders synthesized under precursor concentration of 0.05 M and water content (0 vol%, 5 vol%, 10 vol%, 20 vol%, or 50 vol%). When no water is added (sample 6), the as-synthesized powder consists of only $W_{18}O_{49}$, as suggested by the black spectra in Figure 3. In case of a water content of 5 vol% (sample 7), 10 vol% (sample 8), and 20 vol% (sample 9), as well as of 50 vol% (sample 10), the corresponding diffraction peaks can all be indexed as XRD peaks of γ-WO_3 (see the spectra in Figure 3). This result suggests that the addition of water at this precursor concentration does not stabilize the $WO_3 \cdot 0.33(H_2O)$. A possible explanation is that the γ-WO_3 phase becomes much more stable under high precursor concentration. Based on these results, it can be concluded that the low precursor concentration as well as the appropriate water content are two important (key) parameters to stabilize $WO_3 \cdot 0.33(H_2O)$ in solvothermal synthesis, as shown in Figure 4.

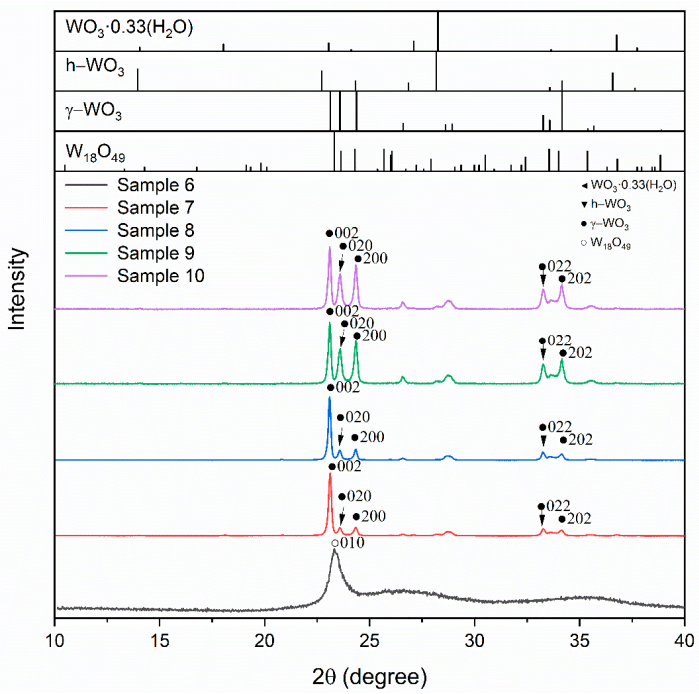

Figure 3. XRD data of samples 6–10 (see details in Table 1). For comparison: the top inset is the standard reference diffraction patterns of $W_{18}O_{49}$ (JCPDS no. 36-0101), h-WO_3 (JCPDS no. 75-2187), $WO_3 \cdot 0.33(H_2O)$ (JCPDS no. 87-1203), and γ-WO_3 (JCPDS no. 32-1295).

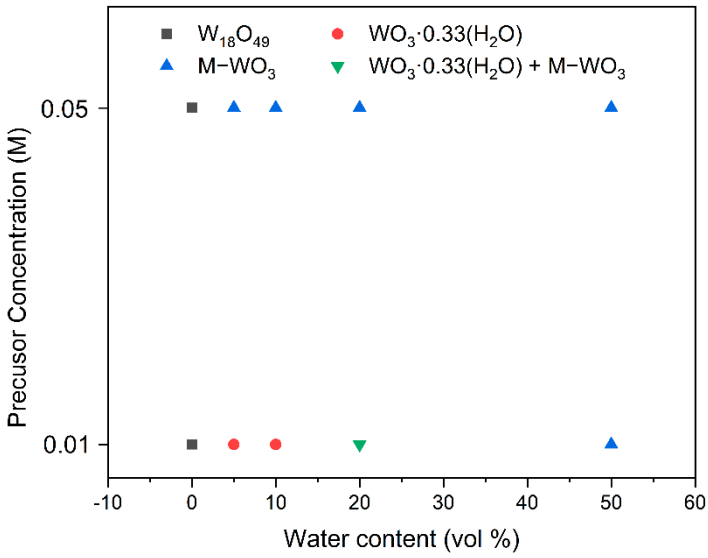

Figure 4. The effect of water content and precursor concentration on the crystal structure of as-synthesized powder.

In addition to identifying the crystal structure by XRD, the particle morphology was explored using detailed SEM (Figure 5) and TEM (Figure 6) characterization. Figure 5a,f (SEM) and Figure 6a,d (TEM) indicate that the crystal morphology of $W_{18}O_{49}$ (i.e., samples 1 and 6) is an urchin-like structure assembled from a bunch of nanorods with an average size of ~10 nm. This then explains the presence of a strong broadening of XRD diffraction peaks observed from sample 1 (Figure 2) and sample 6 (Figure 3). The rate of crystal growth of $W_{18}O_{49}$ seems to be much slower compared to the rate for $WO_3 \cdot 0.33(H_2O)$ and γ-WO_3 crystals. Such a property has been observed before by others [40]. This characteristic might allow the control of the size of a $W_{18}O_{49}$ quantum dot structure as suggested in Ref. [40].

With respect to $WO_3 \cdot 0.33(H_2O)$, Figures 5b,c and 6b show that as-synthesized $WO_3 \cdot 0.33(H_2O)$ powder consists of large faceted platelets with hexagonal shape and an average size of ~5 µm. Such a crystal morphology leads to the presence of dominant facets, i.e., preferential crystallographic orientation (PCO). According to the HRTEM images (Figure 6e) and SAED pattern (insets in Figure 6b), the orientation of the particle along the direction perpendicular to the hexagonal plate is determined to be 002. This can explain the 002 XRD peak of the $WO_3 \cdot 0.33(H_2O)$ (see red or blue curves of Figure 2) having the highest intensity, while the 220 peak in the standard XRD pattern is the strongest peak. The appearance of PCO of $WO_3 \cdot 0.33(H_2O)$ and of the hexagonal-faceted morphology is the result of the natural growth preference of the orthorhombic $WO_3 \cdot 0.33(H_2O)$ structure along six symmetrical directions [41,42].

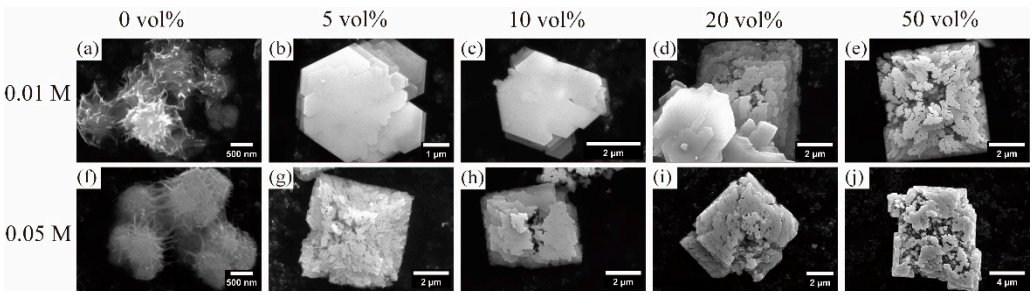

Figure 5. SEM images of samples 1–10 (**a**–**j**).

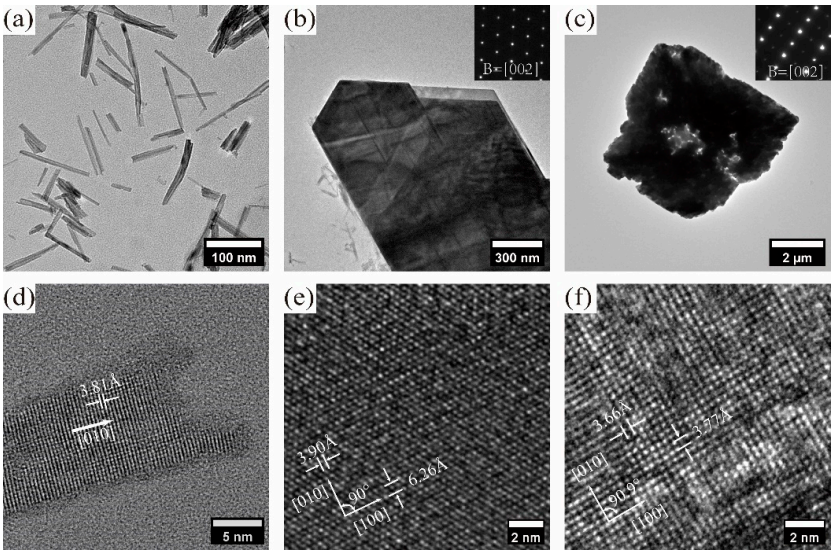

Figure 6. Low-magnification TEM images of (**a**) $W_{18}O_{49}$ (sample 1 and sample 6), (**b**) $WO_3 \cdot 0.33(H_2O)$ (sample 2 and sample 3), and (**c**) γ-WO_3 (sample 5 and samples 7–10); high-resolution TEM images (**d**) $W_{18}O_{49}$ (sample 1 and sample 6), (**e**) $WO_3 \cdot 0.33(H_2O)$ (sample 2 and sample 3), and (**f**) γ-WO_3 (sample 5 and samples 7–10). The inset in (**b**,**c**) is the selected area diffraction pattern.

Figure 5d shows that two kinds of particle are present in sample 4. One type is the $WO_3 \cdot 0.33(H_2O)$ hexagonal-shape particle. The other seems to be a porous sheet with a square shape. As the XRD results shown in Figure 2 suggest that sample 4 consists of both $WO_3 \cdot 0.33(H_2O)$ and γ-WO_3, we postulate that the squared sheet-like particle is a γ-WO_3 particle.

SEM images and XRD results of sample 5 as well as of samples 7–10 confirm this hypothesis. Figure 5e,g–h show that these samples consist of porous squared-sheet particles with an average side length of ~6 μm. Based on XRD results from sample 5 and samples 7–10 indicating the presence of dominantly γ-WO_3, porous square sheets can definitely be identified as γ-WO_3 particles. Similar to the hexagonal-shaped particles, the squared-sheets particles also exhibit PCO. The PCO is determined to be 002 direction by HRTEM images (Figure 6f) and SAED patterns (insets in Figure 6c). This also explains that the 002 XRD peak of as-synthesized γ-WO_3 is the dominant peak (see Figure 2) compared to any other diffraction peaks. According to the Gibbs–Wulff theorem about crystal morphology, the PCO could be attributed to the fact that the 001 facet of γ-WO_3 in ethanol has a lower surface energy [43].

3.2. Effect of Synthesis Temperature and Time on the Synthesis of $WO_3 \cdot 0.33(H_2O)$

The above-presented results suggest that a low precursor concentration and appropriate content of water is critical to obtain $WO_3 \cdot 0.33(H_2O)$ through solvothermal synthesis. Two other important parameters are the synthesis temperature as well as the synthesis time. In a systematic approach to identify the required temperature, the synthesis temperature was varied between 160 °C (sample 11), 180 °C (sample 12), and 200 °C (sample 3) while maintaining all other parameters at a constant, i.e., the water content at 10 vol%, the precursor concentration ([WCl_6]) at 0.01 M, and the synthesis time at 12 h. The XRD results of the as-synthesized powder under these three temperatures are shown in Figure 7, and the results show that the powder synthesized at 160 °C is $W_{18}O_{49}$ and powders synthesized at 180 °C and 200 °C are $WO_3 \cdot 0.33(H_2O)$. Thus, a temperature higher than 180 °C is required to stabilize $WO_3 \cdot 0.33(H_2O)$.

To study the effect of synthesis time, powder was synthesized at 200 °C but for different times. Figure 8 shows the XRD pattern of powder synthesized at 200 °C for 3 h (sample 13), 6 h (sample 14), 9 h (sample 15), and 12 h (sample 3). $W_{18}O_{49}$ and $WO_3 \cdot 0.33(H_2O)$ are both present when a synthesis time of 3 h is selected, as suggested by the black XRD spectra

in Figure 8. Increasing the synthesis time to 6 h results in the increase in the fraction of $WO_3 \cdot 0.33(H_2O)$. When the synthesis time is increased to 9 h and 12 h, the $WO_3 \cdot 0.33(H_2O)$ phase becomes the dominant phase. The presence of the $W_{18}O_{49}$ phase at short synthesis time (3 h and 6 h) can be attributed to an incomplete reaction of water, oxygen, and $W_2Cl_4(OC_2H_5)_6$ due to the insufficient time to fully react. The unreacted precursor finally transforms to $W_{18}O_{49}$ as indicted in XRD pattern when the water content is 0 vol% (samples 1 and 6). An increase in synthesis time results in a decreased fraction of the unreacted precursor, thereby decreasing the fraction of $W_{18}O_{49}$ in the as-synthesized powder.

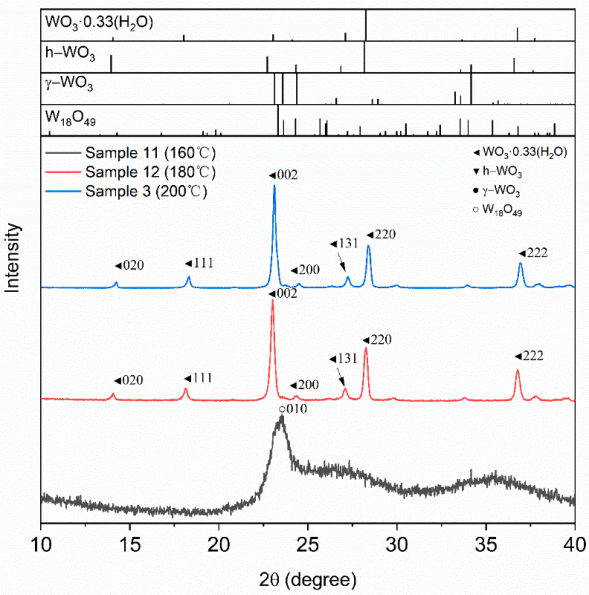

Figure 7. XRD spectra of samples that are synthesized at temperature of 160 °C (sample 11), 180 °C (sample 12), and 200 °C (sample 3), each for 12 h. The top inset is the standard reference diffraction patterns of $W_{18}O_{49}$ (JCPDS no. 36-0101), h-WO_3 (JCPDS no. 75-2187), $WO_3 \cdot 0.33(H_2O)$ (JCPDS no. 87-1203), and γ-WO_3 (JCPDS no. 32-1295).

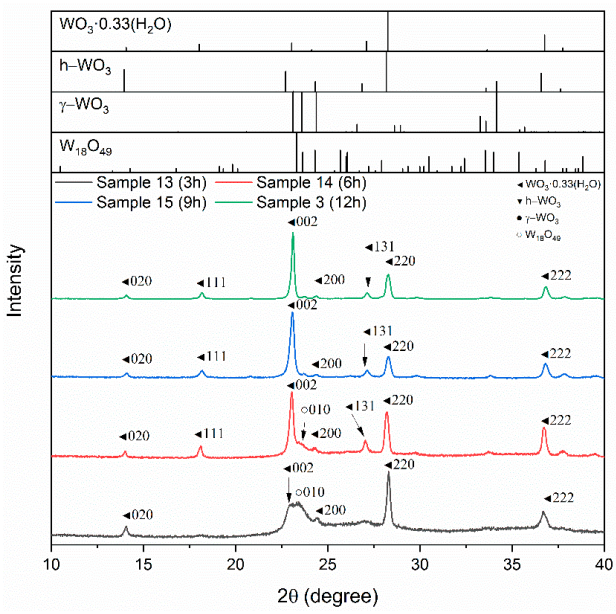

Figure 8. XRD spectra of samples that are synthesized at a temperature of 200 °C, but for 3 h (sample 13), 6 h (sample 14), 9 h (sample 15), and 12 h (sample 3). The top inset is the standard reference diffraction patterns of $W_{18}O_{49}$ (JCPDS no. 36-0101), h-WO_3 (JCPDS no. 75-2187), $WO_3 \cdot 0.33(H_2O)$ (JCPDS no. 87-1203), and γ-WO_3 (JCPDS no. 32-1295).

3.3. Dehydration of $WO_3 \cdot 0.33(H_2O)$

After systematically investigating the effects of synthesis parameters such as precursor concentration, water content, synthesis temperature, and synthesis time for the synthesis of $WO_3 \cdot 0.33(H_2O)$, the next focus is on the transformation of $WO_3 \cdot 0.33(H_2O)$ to hexagonal h-WO_3. This post-synthesis transformation can be achieved by annealing, since $WO_3 \cdot 0.33(H_2O)$ is believed to dehydrate upon heating and the h-WO_3 phase forms at ~350 °C [27–29]. However, the h-WO_3 phase is a metastable phase and is believed to further transform to the thermodynamically stable γ-WO_3 at a temperature between 475–532 °C. The exact temperature of the h-WO_3 to γ-WO_3 phase transformation depends on the purity of the h-WO_3 (e.g., sodium content, ammonium ions content, and so on) [22]. Thus, to determine the exact temperature range to stabilize h-WO_3 for this solvothermal method, thermal gravimetric analysis (TGA) characterization was carried out, and the result is shown in Figure 9. As the TGA curves suggest, the dehydration process starts at 144.3 °C and stops at 505.2 °C. The total weight loss is 2.657%, which is exactly the weight difference between $WO_3 \cdot 0.33(H_2O)$ and WO_3. The first derivative peak temperature (T_p) of dehydration, indicating the point of greatest rate of change on the weight loss curve, is at around 358.6 °C. The highest temperature observed in our study is higher than the temperature reported in previous studies [27–29]. This might be caused by the high ramping rates in our TGA experiments. To determine the best annealing temperature for dehydration, annealing experiments at different temperatures were conducted. Figure 10 shows the XRD pattern of the as-annealed powder. The XRD pattern of the powder annealed at 300 °C and at 350 °C, can be indexed as $WO_3 \cdot 0.33(H_2O)$ plus a minor amount of gamma-WO_3 (the intensity of gamma diffraction peak is too low to be quantified, the fraction is definitely less than 1%). Comparing the spectra at 300 °C (black) and at 350 °C (red), the XRD diffraction peak at 22.98° at 350 °C (red curve) seems to have an asymmetric shape (i.e., slight peak tail at lower 2θ). This indicates that there must be a minor peak present with a θ only slightly less 22.98°. The very low intensity of this peak makes it difficult to determine the exact peak position.

However, this is of less importance here because $WO_3 \cdot 0.33(H_2O)$ is still the dominant phase after annealing at 350 °C for 2 h, which means that this annealing temperature cannot fully transform $WO_3 \cdot 0.33(H_2O)$ to h-WO_3. After the annealing temperature has been increased to 400 °C and to 450 °C, the characteristic XRD peaks of $WO_3 \cdot 0.33(H_2O)$ at 2θ = 18.10° and 22.98° disappear and a new peak at 22.78° appears. This new pattern can be indexed as h-WO_3 (JCPDS no. 75-2187). For the sample annealed at 500 °C, both h-WO_3 and γ-WO_3 XRD diffraction peaks are observed, suggesting that the powder consists of both phases. However, γ-WO_3 dominates when the sample has been annealed at 550 °C. In conclusion, to obtain h-WO_3, the annealing temperature should be kept between 400–450 °C. The morphologies of this annealed powder are also investigated by SEM, and the results are shown in Figure 11. The hexagonal morphology is clearly preserved during the dehydration process, as suggested by the images in Figure 11a–d. This characteristic means that h-WO_3 hexagonal sheet can be obtained via the here presented solvothermal synthesis method. The h-WO_3 hexagonal sheet still has a 002 (0002 for Miller–Bravais indices for hexagonal structure)-preferred orientation, as suggested by the observed XRD pattern. Once the annealing temperature is increased to 500 °C, a change in particle morphology due to the h-WO_3 to γ-WO_3 transformation is observed as shown in Figure 11e–f. The hexagonal sheet seems to decompose into several rods, which presumably are γ-WO_3 phase particles.

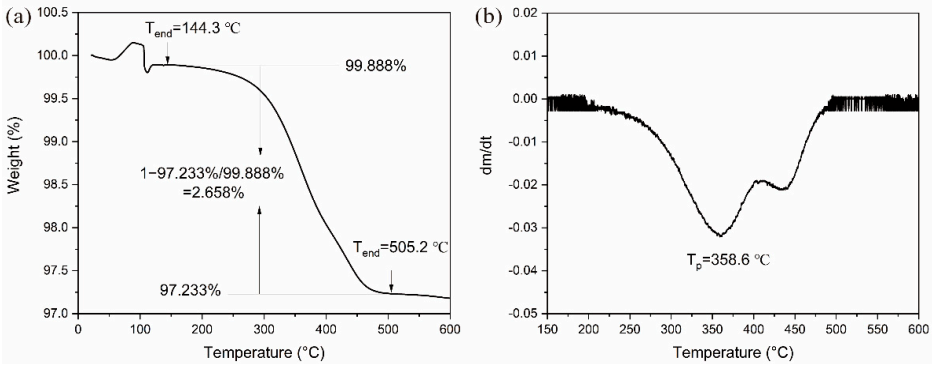

Figure 9. (**a**) TGA curve of $WO_3 \cdot 0.33(H_2O)$; (**b**) the first derivative of TGA curve. The first derivative curve is smoothed by Savitzky-Golay method with window of 20 points.

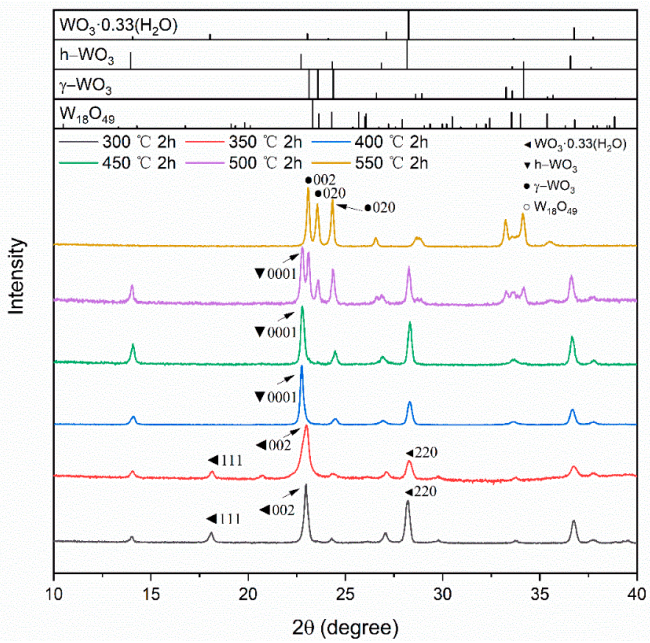

Figure 10. XRD spectra of samples that are annealed at temperature of 300 °C, 350 °C, 400 °C, 450 °C, 500 °C, and 550 °C for 2 h. The starting material is sample no. 3, which only consists of $WO_3 \cdot 0.33(H_2O)$. The top inset is the standard reference diffraction patterns of $W_{18}O_{49}$ (JCPDS no. 36-0101), h-WO_3 (JCPDS no. 75-2187), $WO_3 \cdot 0.33(H_2O)$ (JCPDS no. 87-1203), and γ-WO_3 (JCPDS no. 32-1295).

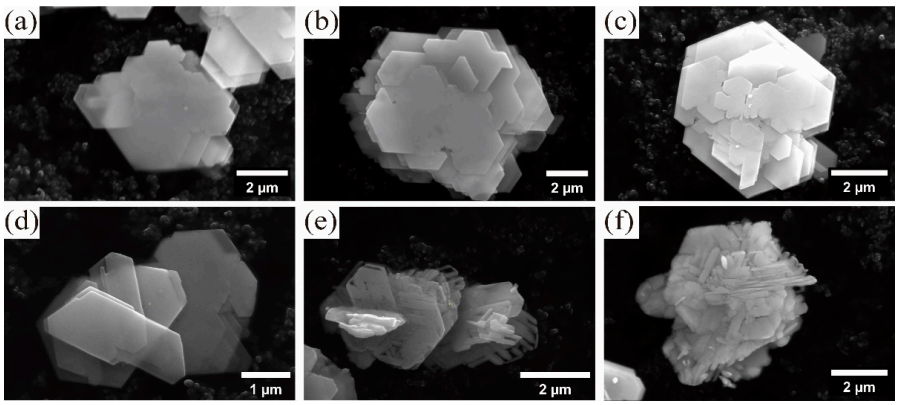

Figure 11. SEM images of powder after annealed at (**a**) 300 °C (**b**) 350 °C (**c**) 400 °C (**d**) 450 °C (**e**) 500 °C, and (**f**) 550 °C.

Summarizing all the results presented here, we are now able to outline a two-step procedure to obtain metastable h-WO_3 using a solvothermal route followed by a post-synthesis high temperature annealing:

- First, $WO_3 \cdot 0.33(H_2O)$ should be synthesized by a solvothermal process. To ensure no other phase is produced, the WCl_6 concentration should be as low as 0.01 M, the water content should be between 5–10 vol%, the synthesis temperature should be higher than 180 °C, and the synthesis time should be longer than 9 h;
- Then, in the subsequent annealing process, the $WO_3 \cdot 0.33(H_2O)$ is transformed to h-WO_3. In order to stabilize the metastable hexagonal structure, the annealing temperature needs to be carefully controlled between 400 °C and 450 °C.

4. Conclusions

The metastable hexagonal tungsten trioxide phase (h-WO_3) was successfully synthesized via a solvothermal synthesis followed by a controlled annealing step. The $WO_3 \cdot 0.33(H_2O)$ is first synthesized in a solvothermal process and subsequent annealing triggers the dehydration of $WO_3 \cdot 0.33(H_2O)$, thereby transforming $WO_3 \cdot 0.33(H_2O)$ to h-WO_3. Compared with previously published studies on solvothermal synthesis of h-WO_3, our study has resolved the ambiguity of the product of solvothermal synthesis of h-WO_3. The impact of several synthesis parameters are more evident now as they have been studied systematically.

- Parameters of the solvothermal process: WCl_6 precursor concentration as low as 0.01 M, water content 5–10 vol%, synthesis temperature higher than 180 °C, synthesis time longer than 9 h;
- Parameters of the subsequent annealing process: annealing temperature between 400 °C and 450 °C.

In addition, the following important dependencies on synthesis parameters were found:

(i) Higher WCl_6 precursor concentration and higher water content in the solvent results in formation of thermostable γ-WO_3 with porous squared-sheet morphology. The preferential crystallographic orientation of the γ-WO_3 nanosheet is 002 orientation. Precursor concentration of 0.01 M and water content of 5–10 vol% produce pure 002-orientated $WO_3 \cdot 0.33(H_2O)$ hexagonal nanosheets. The urchin-like $W_{18}O_{49}$ is only present when water is absent from the solvent;

(ii) Synthesis temperature below 180 °C and synthesis time below 6 h might also result in the formation of $W_{18}O_{49}$ and, therefore, should be avoided. This is attributed to the insufficient reaction caused by low synthesis temperature and short synthesis time;

(iii) Annealing at temperature higher than 400 °C is required to dehydrate the $WO_3 \cdot 0.33$ (H_2O) and produce h-WO_3. However, annealing time higher than 500 °C results in a h to γ transition. The dehydration process does not destroy the hexagonal morphology of the particle and, thus, the h-WO_3 hexagonal sheet can be produced.

Further work is focused on studying the purity of the h-WO_3 synthesized here, including the amount and level of structural defects, as well as on upscaling this two-step process to produce h-WO_3 and exploring the wide range of applications, e.g., in gas sensors or photocatalysts.

Author Contributions: Conceptualization, Z.Q. and P.-I.G.; methodology, Z.Q.; software, Z.Q.; validation, Z.Q., J.R.J. and P.-I.G.; formal analysis, Z.Q., J.R.J. and P.-I.G.; investigation, Z.Q.; resources, J.R.J. and P.-I.G.; data curation, Z.Q.; writing—original draft preparation, Z.Q.; writing—review and editing, Z.Q., J.R.J. and P.-I.G.; visualization, Z.Q.; supervision, J.R.J. and P.-I.G.; project administration, J.R.J. and P.-I.G.; funding acquisition, P.-I.G. All authors have read and agreed to the published version of the manuscript.

Funding: This research has received funding by the Orton Chair Funds and the National Science Foundation award CBET #2029847.

Data Availability Statement: Not applicable.

Acknowledgments: The authors would like to thank the Center for Electron Microscopy and Analysis (CEMAS) as the XRD and electron microscopy characterization were performed at the Center for Electron Microscopy and Analysis (CEMAS) at the Ohio State University.

Conflicts of Interest: The authors declare that they have no known competing financial interests or personal relationships that could appear to influence the work reported in this paper.

References

1. Christopher, J.H.; Vittorio, L.; Kevin, S.K. High-temperature phase transitions in tungsten trioxide—The last word? *J. Phys. Condens. Matter* **2002**, *14*, 377. [CrossRef]
2. Han, W.; Shi, Q.; Hu, R. Advances in Electrochemical Energy Devices Constructed with Tungsten Oxide-Based Nanomaterials. *Nanomaterials* **2021**, *11*, 692. [CrossRef] [PubMed]
3. Sood, S.; Gouma, P. Polymorphism in nanocrystalline binary metal oxides. *Nanomater. Energy* **2013**, *2*, 82–96. [CrossRef]
4. Szilágyi, I.M.; Madarász, J.; Pokol, G.; Király, P.; Tárkányi, G.; Saukko, S.; Mizsei, J.; Tóth, A.L.; Szabó, A.; Varga-Josepovits, K. Stability and Controlled Composition of Hexagonal WO_3. *Chem. Mater.* **2008**, *20*, 4116–4125. [CrossRef]
5. Sun, W.; Yeung, M.T.; Lech, A.T.; Lin, C.W.; Lee, C.; Li, T.; Duan, X.; Zhou, J.; Kaner, R.B. High Surface Area Tunnels in Hexagonal WO_3. *Nano Lett.* **2015**, *15*, 4834–4838. [CrossRef]
6. Adhikari, S.; Sarkar, D. High Efficient Electrochromic WO_3 Nanofibers. *Electrochim. Acta* **2014**, *138*, 115–123. [CrossRef]
7. Balázsi, C.; Sedlácková, K.; Pfeifer, J.; Tóth, A.L.; Zayim, E.O.; Szilágyi, I.M.; Wang, L.; Kalyanasundaram, K.; Gouma, P.-I. Synthesis and Examination of Hexagonal Tungsten Oxide Nanocrystals for Electrochromic and Sensing Applications. In *Sensors for Environment, Health and Security: Advanced Materials and Technologies*; Springer: Dordrecht, The Netherlands, 2009; pp. 77–91.
8. Abe, O.O.; Qiu, Z.; Jinschek, J.R.; Gouma, P.-I. Effect of (100) and (001) Hexagonal WO_3 Faceting on Isoprene and Acetone Gas Selectivity. *Sensors* **2021**, *21*, 1690. [CrossRef] [PubMed]
9. Gouma, P.I.; Wang, L.; Simon, S.R.; Stanacevic, M. Novel Isoprene Sensor for a Flu Virus Breath Monitor. *Sensors* **2017**, *17*, 199. [CrossRef]
10. Zhang, D.; Fan, Y.; Li, G.; Ma, Z.; Wang, X.; Cheng, Z.; Xu, J. Highly sensitive BTEX sensors based on hexagonal WO_3 nanosheets. *Sens. Actuators B Chem.* **2019**, *293*, 23–30. [CrossRef]
11. Mohamed, M.M.; Salama, T.M.; Hegazy, M.A.; Abou Shahba, R.M.; Mohamed, S.H. Synthesis of hexagonal WO_3 nanocrystals with various morphologies and their enhanced electrocatalytic activities toward hydrogen evolution. *Int. J. Hydrogen Energy* **2019**, *44*, 4724–4736. [CrossRef]
12. Peng, T.; Ke, D.; Xiao, J.; Wang, L.; Hu, J.; Zan, L. Hexagonal phase WO_3 nanorods: Hydrothermal preparation, formation mechanism and its photocatalytic O2 production under visible-light irradiation. *J. Solid State Chem.* **2012**, *194*, 250–256. [CrossRef]
13. Pang, H.-F.; Xiang, X.; Li, Z.-J.; Fu, Y.-Q.; Zu, X.-T. Hydrothermal synthesis and optical properties of hexagonal tungsten oxide nanocrystals assisted by ammonium tartrate. *Phys. Status Solidi A* **2012**, *209*, 537–544. [CrossRef]
14. Zakharova, G.S.; Podval'naya, N.y.V.; Gorbunova, T.y.I.; Pervova, M.G.; Murzakaev, A.M.; Enyashin, A.N. Morphology-controlling hydrothermal synthesis of h-WO_3 for photocatalytic degradation of 1,2,4-trichlorobenzene. *J. Alloys Compd.* **2023**, *938*, 168620. [CrossRef]
15. Bhojane, P.; Shirage, P.M. Facile preparation of hexagonal WO_3 nanopillars and its reduced graphene oxide nanocomposites for high-performance supercapacitor. *J. Energy Storage* **2022**, *55*, 105649. [CrossRef]
16. Nekita, S.; Nagashima, K.; Zhang, G.; Wang, Q.; Kanai, M.; Takahashi, T.; Hosomi, T.; Nakamura, K.; Okuyama, T.; Yanagida, T. Face-Selective Crystal Growth of Hydrothermal Tungsten Oxide Nanowires for Sensing Volatile Molecules. *ACS Appl. Nano Mater.* **2020**, *3*, 10252–10260. [CrossRef]
17. Ahmadian, H.; Tehrani, F.S.; Aliannezhadi, M. Hydrothermal synthesis and characterization of WO_3 nanostructures: Effects of capping agent and pH. *Mater. Res. Express* **2019**, *6*, 105024. [CrossRef]
18. Marques, A.C.; Santos, L.; Costa, M.N.; Dantas, J.M.; Duarte, P.; Goncalves, A.; Martins, R.; Salgueiro, C.A.; Fortunato, E. Office paper platform for bioelectrochromic detection of electrochemically active bacteria using tungsten trioxide nanoprobes. *Sci. Rep.* **2015**, *5*, 9910. [CrossRef]
19. Wenderich, K.; Noack, J.; Kärgel, A.; Trunschke, A.; Mul, G. Effect of Temperature and pH on Phase Transformations in Citric Acid Mediated Hydrothermal Growth of Tungsten Oxide. *Eur. J. Inorg. Chem.* **2018**, *2018*, 917–923. [CrossRef]
20. Zheng, J.Y.; Haider, Z.; Van, T.K.; Pawar, A.U.; Kang, M.J.; Kim, C.W.; Kang, Y.S. Tuning of the crystal engineering and photoelectrochemical properties of crystalline tungsten oxide for optoelectronic device applications. *CrystEngComm* **2015**, *17*, 6070–6093. [CrossRef]
21. Szilágyi, I.M.; Wang, L.; Gouma, P.-I.; Balázsi, C.; Madarász, J.; Pokol, G. Preparation of hexagonal WO_3 from hexagonal ammonium tungsten bronze for sensing NH_3. *Mater. Res. Bull.* **2009**, *44*, 505–508. [CrossRef]
22. Szilágyi, I.M.; Pfeifer, J.; Balázsi, C.; Tóth, A.L.; Varga-Josepovits, K.; Madarász, J.; Pokol, G. Thermal stability of hexagonal tungsten trioxide in air. *J. Therm. Anal. Calorim.* **2008**, *94*, 499–505. [CrossRef]
23. Abbaspoor, M.; Aliannezhadi, M.; Tehrani, F.S. Effect of solution pH on as-synthesized and calcined WO_3 nanoparticles synthesized using sol-gel method. *Opt. Mater.* **2021**, *121*, 111552. [CrossRef]

24. Gouma, P.I.; Kalyanasundaram, K. Novel synthesis of hexagonal WO_3 nanostructures. *J. Mater. Sci.* **2015**, *50*, 3517–3522. [CrossRef]
25. Kharade, R.R.; Patil, K.R.; Patil, P.S.; Bhosale, P.N. Novel microwave assisted sol–gel synthesis (MW-SGS) and electrochromic performance of petal like h-WO_3 thin films. *Mater. Res. Bull.* **2012**, *47*, 1787–1793. [CrossRef]
26. Cremonesi, A.; Bersani, D.; Lottici, P.P.; Djaoued, Y.; Ashrit, P.V. WO_3 thin films by sol–gel for electrochromic applications. *J. Non-Cryst. Solids* **2004**, *345–346*, 500–504. [CrossRef]
27. Perfecto, T.M.; Zito, C.A.; Volanti, D.P. Room-temperature volatile organic compounds sensing based on $WO_3 \cdot 0.33H_2O$, hexagonal-WO_3, and their reduced graphene oxide composites. *RSC Adv.* **2016**, *6*, 105171–105179. [CrossRef]
28. Seguin, L.; Figlarz, M.; Pannetier, J. A novel supermetastable WO_3 phase. *Solid State Ion.* **1993**, *63–65*, 437–441. [CrossRef]
29. Figlarz, M. New oxides in the WO_3-MoO_3 system. *Prog. Solid State Chem.* **1989**, *19*, 1–46. [CrossRef]
30. Choi, H.G.; Jung, Y.H.; Kim, D.K. Solvothermal Synthesis of Tungsten Oxide Nanorod/Nanowire/Nanosheet. *J. Am. Ceram. Soc.* **2005**, *88*, 1684–1686. [CrossRef]
31. Chacón, C.; Rodríguez-Pérez, M.; Oskam, G.; Rodríguez-Gattorno, G. Synthesis and characterization of WO_3 polymorphs: Monoclinic, orthorhombic and hexagonal structures. *J. Mater. Sci. Mater. Electron.* **2014**, *26*, 5526–5531. [CrossRef]
32. Ortega, J.M.; Martínez, A.I.; Acosta, D.R.; Magaña, C.R. Structural and electrochemical studies of WO_3 films deposited by pulsed spray pyrolysis. *Sol. Energy Mater. Sol. Cells* **2006**, *90*, 2471–2479. [CrossRef]
33. Wu, P.M.; Ishii, S.; Tanabe, K.; Munakata, K.; Hammond, R.H.; Tokiwa, K.; Geballe, T.H.; Beasley, M.R. Synthesis and ionic liquid gating of hexagonal WO_3 thin films. *Appl. Phys. Lett.* **2015**, *106*, 042602. [CrossRef]
34. Huang, K.; Pan, Q.; Yang, F.; Ni, S.; Wei, X.; He, D. Controllable synthesis of hexagonal WO_3 nanostructures and their application in lithium batteries. *J. Phys. D Appl. Phys.* **2008**, *41*, 155417. [CrossRef]
35. Miao, B.; Zeng, W.; Hussain, S.; Mei, Q.; Xu, S.; Zhang, H.; Li, Y.; Li, T. Large scale hydrothermal synthesis of monodisperse hexagonal WO_3 nanowire and the growth mechanism. *Mater. Lett.* **2015**, *147*, 12–15. [CrossRef]
36. Ghosh, K.; Roy, A.; Tripathi, S.; Ghule, S.; Singh, A.K.; Ravishankar, N. Insights into nucleation, growth and phase selection of WO_3: Morphology control and electrochromic properties. *J. Mater. Chem. C* **2017**, *5*, 7307–7316. [CrossRef]
37. Lu, Y.; Zhang, J.; Wang, F.; Chen, X.; Feng, Z.; Li, C. K2SO4-Assisted Hexagonal/Monoclinic WO_3 Phase Junction for Efficient Photocatalytic Degradation of RhB. *ACS Appl. Energy Mater.* **2018**, *1*, 2067–2077. [CrossRef]
38. Li, C.-P.; Lin, F.; Richards, R.M.; Engtrakul, C.; Tenent, R.C.; Wolden, C.A. The influence of sol–gel processing on the electrochromic properties of mesoporous WO_3 films produced by ultrasonic spray deposition. *Sol. Energy Mater. Sol. Cells* **2014**, *121*, 163–170. [CrossRef]
39. Li, Y.; Tang, Z.; Zhang, J.; Zhang, Z. Exposed facet and crystal phase tuning of hierarchical tungsten oxide nanostructures and their enhanced visible-light-driven photocatalytic performance. *CrystEngComm* **2015**, *17*, 9102–9110. [CrossRef]
40. Wang, Y.; Wang, X.; Xu, Y.; Chen, T.; Liu, M.; Niu, F.; Wei, S.; Liu, J. Simultaneous Synthesis of WO_{3-x} Quantum Dots and Bundle-Like Nanowires Using a One-Pot Template-Free Solvothermal Strategy and Their Versatile Applications. *Small* **2017**, *13*, 1603689. [CrossRef]
41. Li, J.; Huang, J.; Wu, J.; Cao, L.; Li, Q.; Yanagisawa, K. Microwave-assisted growth of $WO_3 \cdot 0.33H_2O$ micro/nanostructures with enhanced visible light photocatalytic properties. *CrystEngComm* **2013**, *15*, 7904–7913. [CrossRef]
42. Li, J.; Huang, J.; Yu, C.; Wu, J.; Cao, L.; Yanagisawa, K. Hierarchically Structured Snowflakelike $WO_3 \cdot 0.33H_2O$ Particles Prepared by a Facile, Green, and Microwave-assisted Method. *Chem. Lett.* **2011**, *40*, 579–581. [CrossRef]
43. Gadewar, S.B.; Hofmann, H.M.; Doherty, M.F. Evolution of Crystal Shape. *Cryst. Growth Des.* **2004**, *4*, 109–112. [CrossRef]